Microsc. Microanal. 12, 97–105, 2006
DOI: 10.1017/S1431927606060168

Microscopy AND Microanalysis

Three-Dimensional Characterization of Cell Clusters Using Synchrotron-Radiation-Based Micro-Computed Tomography

Bert Müller,[1,*] Marco Riedel,[2] Philipp J. Thurner[1,3]

[1]*Computer Vision Laboratory ETH Zürich, Gloriastrasse 35, CH-8092 Zürich, Switzerland*
[2]*ProBioGen, Sternwartstrasse 7, D-13086 Berlin, Germany*
[3]*Swiss Federal Institute for Materials Testing and Research, Überlandstrasse 129, CH-8600 Dübendorf, Switzerland*

Abstract: Micro-computed tomography with the highly intense, monochromatic X rays produced by the synchrotron is a superior method to nondestructively measure the local absorption in three-dimensional space. Because biological tissues and cells consist mainly of water as the surrounding medium, higher absorbing agents have to be incorporated into the structures of interest. Even without X-ray optics such as refractive lens, one can uncover the stain distribution with the spatial resolution of about 1 μm. Incorporating the stain at selected cell compartments, for example, binding to the RNA/DNA, their density distribution becomes quantified. In this communication, we demonstrate that tomograms obtained at the beamlines BW2 and W2 (HASYLAB at DESY, Hamburg, Germany) and 4S (SLS, Villigen, Switzerland) clearly show that the RNA/DNA-stained HEK 293 cell clusters have a core of high density and a peripheral part of lower density, which correlate with results of optical microscopy. The inner part of the clusters is associated with nonvital cells as the result of insufficient oxygen and nutrition supply. This necrotic part is surrounded by (6 ± 1) layers of vital cells.

Key words: micro-computed tomography, synchrotron radiation, HEK 293 cell cluster, DNA/RNA staining, 3D characterization, segmentation

Introduction

Human tissue is usually organized in the three-dimensional (3D) space. Nevertheless, most of the *in vitro* studies with cells are simply performed in petri dishes with flat layers of cells just in two dimensions. Only recently (Abbott & Cyranoski, 2003; Takezawa, 2003) has it been realized that cells cultured in the *in vivo*-like 3D fashion behave differently from those that are kept as single cells or as monolayers, although selected articles were published earlier (see Hoffman, 1993). The importance of the third dimension in cell and molecular biology becomes clearer. One of the first prominent examples is the behavior of cancerous breast cells (Weaver et al., 1997), which change their shape and their growth in three dimensions with respect to the 2D culture. They even seem to become noncancerous. Fetal rat lung cells are another example. If stress is physiologically applied to the cultures, no reaction on mechanical load is detected for the 2D monolayer, whereas a significant reaction is found for the organo-typic 3D configuration (Liu et al., 1995). Furthermore, it is known that liver cells, which spread out on different templates, lose their functionality (Müller & Wintermantel, 1999). Cells of 3D histoids, however, are rounded and show a gene expression much closer to the *in vivo* situation (Hoffman, 1993). Therefore, the most relevant *in vitro* studies on tissue formation should be conducted in an environment in which cellular responses can be studied in the 3D organo-mimetic architecture. The cells need the contact with each other and the support of the extracellular matrix (ECM). The ECM contains many proteins to organize the communication between the cells and determines the (mechanical) properties of the histoids.

The morphological characterization of the cells is generally carried out by 2D microscopy techniques. The reason lies in the lack of appropriate methods to make the 3D cell arrangements visible with equidistant resolution in the three orthogonal dimensions. Although confocal laser scanning microscopy (CLSM) seems to be suitable for 3D cell culture visualization (Laurent et al., 1994), the spatial resolution in the third dimension including their calibration is often unsatisfying. In addition, the information depth is limited. Even more important, cells within opaque scaffolds are impossible to access by CLSM.

Received July 20, 2004; accepted September 8, 2005.
*Corresponding author. E-mail: bmueller@vision.ee.ethz.ch

As an alternative, we propose synchrotron-radiation-based micro-computed tomography (SRμCT) to make visible the 3D arrangement of cells in submillimeter cell clusters of spheroid and toroid shape. Because the cells consist mainly of water as the surrounding medium, they must be stained with contrast agents for visualization in absorption contrast mode. In our previous publication the strong absorbing agents (osmium, gold) are bonded to the fibroblasts in a rather unspecific way mostly to the cell membranes (Thurner et al., 2003). Therefore, only quantitative information on the entire cell culture was extracted, but the segmentation of individual cells was unachievable. Here, human embryonic kidney cells from the cell line HEK 293 have been investigated, whereby we have incorporated different protocols. Besides the unspecific staining, a protocol is applied to stain the DNA and RNA by osmium (Levin-Zaidman et al., 2000). According to the protocol most of the osmium should be concentrated in the nuclei. Thus, the procedure might be termed *nucleus staining*. The extraction of the local RNA/DNA density might indicate the functionality of the cells in the 3D cluster (Müller-Klieser, 1987; König et al., 1991). The SRμCT measurement of the spatial stain distribution directly relates to the RNA/DNA density. The local absorption values quantified by SRμCT are subsequently compared with the 2D microscopic images and the results of cluster histology. The main advantages of SRμCT with respect to classical histology are the exclusion of the preparation artifacts and the fully 3D character of the retrieved data. The virtual cuts for visualization and quantification purposes can be freely chosen. Therefore, representative cuts can be selected, which is not *a priori* given by classical histology, because the histological cut is usually not exactly perpendicular to the surface of the cell clusters, and rim structure thicknesses are generally overestimated. Conversely, the almost isotropic spatial resolution and the cubic voxel geometry in SRμCT allow the quantitative assessment of the 3D data sets (Hildebrand & Rüegsegger, 1997). The numerical evaluation procedures are often automated and provide parameters with high statistical relevance (Bernhardt et al., 2004).

Materials and Methods

Cell Cluster Preparation

For the experiments, relatively large cell clusters of millimeter and submillimeter size, which could be regarded as a pre-state of tissue, were prepared. The human embryonic kidney cell line HEK 293 was cultivated in a serum-free basal medium (PBG1.0, PERBIO, Sweden). The medium was supplemented with 8 mM L-glutamine, 8 μg/mL insulin, and a mixture of sodium hypoxanthine and thymidine (HT Supplement 1X, Invitrogen, Inc.). Here, the spheroids of (sub)millimeter size were formed during a cultivation time of up to 13 weeks.

Standard Characterization of the Cell Clusters

After preparation the spheroids were characterized by microscopic methods. Optical microscopy was performed using the inverse microscope IX-50 equipped with a Hoffman-Modulator (Olympus GmbH). For fluorescence imaging, the cells were stained by the mixture of propidium iodide (PI) (1 μg/mL; Sigma) and fluorescein diacetate (FDA; 0.5 μM, Mw 416.4 g/mol; Lot 89H5077, Sigma) added to the cell culture.

Cell Cluster Staining

For the unspecific staining, the clusters were taken from the T-flask and fixated with 0.5% glutaraldehyde (25% in water; Lot S35131, VWR) for 3 h at a temperature of 4°C. After that, cell clusters were slightly washed with cacodylate buffer (0.1 M sodium cacodylate trihydrate, pH 7.4; Lot K30262856 209, VWR) and the postfixation was made with 0.1 mL cacodylate buffer and 0.1 mL 2% osmium tetroxide (lot L457066 203, VWR) for 1 h at room temperature.

For the final embedding, the clusters were rinsed with the cacodylate buffer. Subsequently, they were embedded in a thin-walled glass capillary using the JB-4 Plus embedding kit (designed for histology; lot 523142, Polysciences, Inc.) and held at room temperature for a duration of at least 24 h.

To stain the RNA and DNA of the HEK 293 cells, different preparation steps were carried out. First, the cell clusters were slightly washed with cacodylate buffer (0.1 M sodium cacodylate trihydrate, pH 7.4; lot K30262856 209, VWR). Second, the staining solution of osmiumammine-B was added as described by Levin-Zaidman et al. (2000). For this preparation step, 0.4% osmiumammine-B (lot 526789, Polysciences, Inc.) in 40 mM sodium metabisulfite (97+%; lot AA15129MO, Aldrich) with 8 M acetic acid (p.a.; lot K32207563, VWR) was dissolved. Finally, the cell clusters were incubated with the staining solution for 1 h at room temperature, rinsed with cacodylate buffer and incubated for additional 2 h.

For embedding here, the samples were incubated for 2 h with the infiltration solution (Technovit 7100; Lot 010253, Heraeus Kulzer GmbH). Subsequently, the hardener (6.7 mL hardener to 100 mL infiltration solution; Lot 010149, Heraeus Kulzer GmbH) was added, and the embedded cell clusters were immediately put into a Teflon tube 2 mm in diameter. After storage for 1 day, the preparation procedure was finalized.

Synchrotron-Radiation-Based Micro-Computed Tomography

Prior to tomographic scanning, the samples were extracted from the glass and Teflon tubes, respectively, and glued onto the sample holders. The samples had been exactly positioned on the rotation stage to guarantee the illumination and registration of the whole sample diameter during the

acquisition of the projections. The SRμCT measurements were carried out at the beamlines BW2 and W2 (HASYLAB at DESY, Hamburg, Germany), that is, a synchrotron radiation source of the second generation (Beckmann, 2001), and the materials science beamline 4S (SLS at PSI, Villigen, Switzerland), a synchrotron radiation source of the third generation, with the standard setup for absorption contrast (Stampanoni et al., 2001). Because the synchrotron radiation exhibits only a very small divergence, the X rays are almost parallel, and the tomogram can be reconstructed slice by slice. The reconstruction is based on the filtered back-projection algorithm (Kak & Slaney, 2001) using the Buter filter.

For the characterization of the sample with the unspecific stain at the beamline BW2 (HASYLAB at DESY) the photon energy was set to 14.5 keV. Three hundred and sixty projections between 0° and 180° were recorded with an optical magnification of 6.08, resulting in a pixel length of 1.48 μm. Subsequently, the same sample was measured at the materials science beamline 4S (SLS at PSI) using 1000 projections at the photon energy of 10.0 keV. The pixel length corresponds to 0.70 μm, but to improve the density resolution (Thurner et al., 2004) and for better comparability, the projections were binned with a factor of 2, which gives rise to a pixel length of 1.40 μm.

For the characterization of the nucleus stained samples at the beamline W2 (HASYLAB at DESY) a photon energy of 22.0 keV was selected. Seven hundred and twenty projections with an optical magnification of 4.45, which leads to a pixel length of 2.02 μm, were recorded. At the beamline 4S (SLS at PSI) the photon energy was 12.0 keV. Twelve hundred projections were recorded with a pixel length of 1.75 μm.

Image Processing

The SRμCT tomograms from the beamline BW2 (HASYLAB at DESY) led to histograms of the local absorption coefficients that have exactly a Gaussian shape (Müller et al., 2002). Therefore, it should be rather simple to determine the threshold for the segmentation of the stained cellular material. The histograms extracted from the different tomograms after Gauss fitting were approximated with three Gaussians by the use of the Levenberg–Marquardt algorithm (Marquardt, 1969) of the proFit code (proFit 5.6.4; Quantumsoft, Zurich, Switzerland). The thresholds for the different phases were always set at the intersection points of the Gaussians for the adjacent phases. After the thresholding for the selected entire cell cluster (including the partial volume in the case of the OsO_4-stained clusters) the component labeling (Suzuki et al., 2003) was performed omitting all components except the largest one. The component-labeled volume was used to mask the original data set to retrieve the distribution of the absorption coefficients only within the respective cell cluster. For the 3D visualization of the cell clusters the software VG Studio Max (Volume Graphics, Heidelberg, Germany) was used. The interactive data language, IDL (Research Systems Inc., USA), served for the more detailed quantitative analysis of the tomograms.

Results

Figure 1 shows the 3D representation of a HEK 293 cell cluster of almost spheroid shape, which is about half a millimeter long. A part of the cluster is marked by white instead of the yellow color to better demonstrate that cell-like structures might be identified at the cluster's surface. The contrast and the spatial resolution, however, are insufficient to segment the majority of individual cells from the cluster's surface. The representation is based on the tomogram obtained at the beamline 4S. To increase the density resolution at the expense of the spatial resolution (Thurner et al., 2004), the 3D representation in Figure 1 is based on a binning factor of 3. This means that the voxel length corresponds to 2.1 μm. Assuming a typical diameter of 10 μm for the individual HEK 293 cells, each cell is composed of about 100 voxels. Note that the number of cells forming the cluster is between 10^4 and 10^5, if the same assumption is applied.

To get an insight into the cell cluster, the same cluster is shown in Figure 2 virtually cut into two fragments. Inside the cluster, individual cells cannot be identified. The density, characterized by the yellow-red color, seems to be inhomogeneous but more or less constant from the center to the periphery. The color bar is chosen according to the histogram of the absorption values, shown in Figure 3. The histograms from the tomograms obtained at the beamlines BW2 (HASYLAB at DESY) and 4S (SLS) at different photon energies exhibit two well-separated peaks with some overlap. The dominant peak represents the embedding material. The other peak is associated with the stained cells. As expected for the measurements at the beamline BW2 (HASYLAB at DESY) (Müller et al., 2002), the peaks have exactly a Gaussian shape. At the interface between the cell cluster and the bare embedding the partial volume effects occur, which are characterized by the green color bar. These intermediate absorption values are determined by the intersections using the third Gaussian and are indeed found at the periphery of the cell cluster (cf. Figs. 2 and 3). The white-colored line on top of the data points is the superposition of the three Gaussians and demonstrates that the histograms can be perfectly described by such a fit for both SRμCT measurements. The slightly smaller values of the full width at half maximum (FWHM) relative to the peak separations are a strong indication for the better density resolution in the tomogram acquired at the SLS with respect to the one of the HASYLAB. On the right-hand side of Figure 3 typical slices of the same cluster measured at the different synchrotron radiation sources are reproduced. The

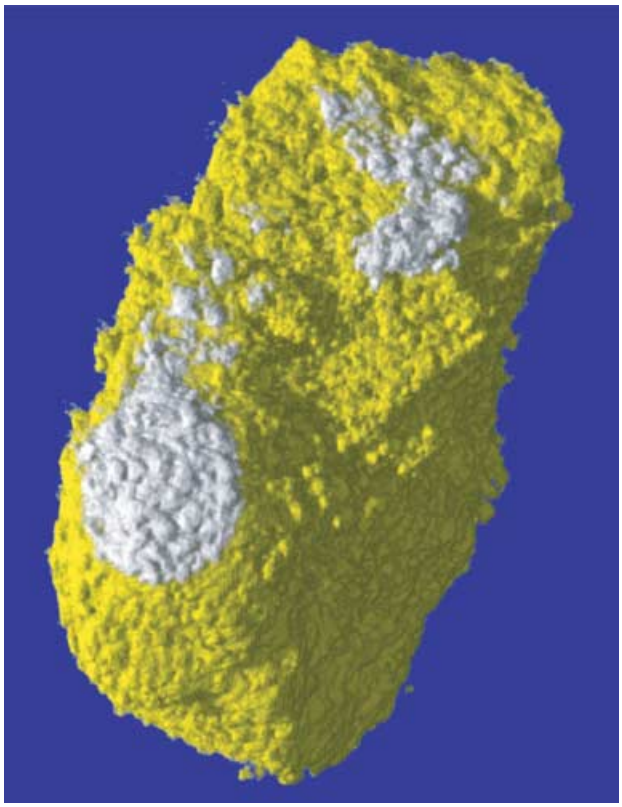

Figure 1. *See caption on facing page.*

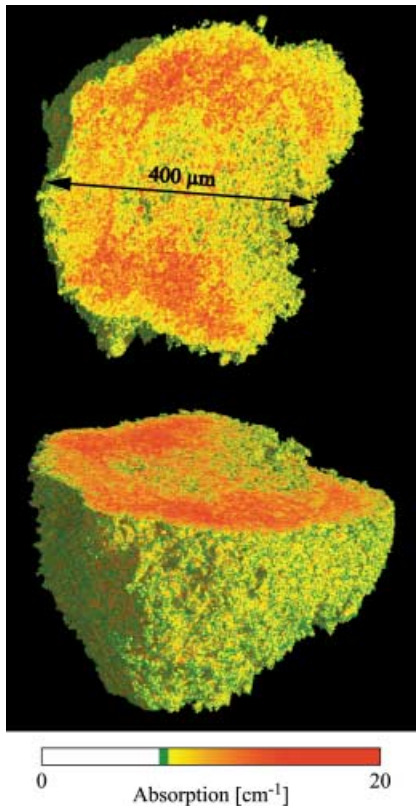

Figure 2. *See caption on facing page.*

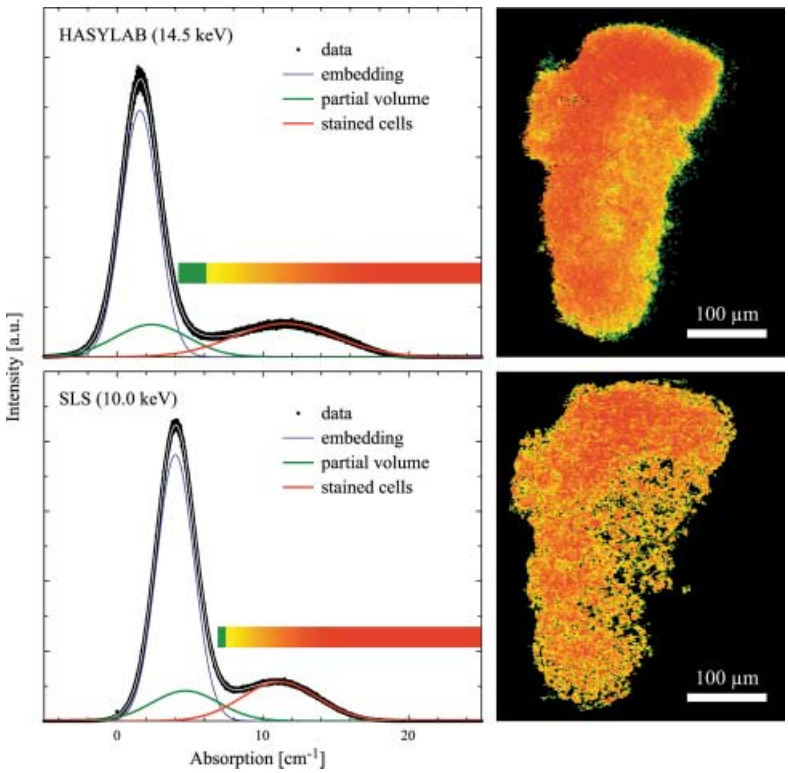

Figure 3. The histograms of the local absorption values can be perfectly fitted by 3 Gaussians (white line on top of the black dots characterizing the data). Note the similarities between both diagrams obtained from tomograms of very different synchrotron radiation sources: second and third generation, respectively. The higher absorption values for the data of the SLS are the result of the lower photon energy. The slices on the right-hand side are not exactly in the same orientation, but they clearly indicate the better image quality of the third-generation synchrotron radiation source. Here, in some areas of lower cell density, features with a diameter of about 10 μm associated with individual cells could be extracted.

Figure 1. The cluster of 10^4 to 10^5 HEK 293 cells, which is about 0.5 mm long, shows that SRμCT might uncover cell-like structures. The white areas instead of the yellow color should support the impression. The data are visualized from a tomogram obtained at the materials science beamline 4S (SLS, PSI, Switzerland) using a photon energy of 10.0 keV. To increase the density resolution (contrast), the data are binned by a factor of 3.

Figure 2. The virtual cut of the cell cluster shown in Figure 1 also gives the impression that at least in the low-density region individual cells might be uncovered. The computational analysis, however, indicates an inhomogeneous distribution more or less constant over the entire cluster. The partial volume effect at the interface between cells and embedding material becomes visible by the green color. The color bar is chosen according to the one in Figure 3.

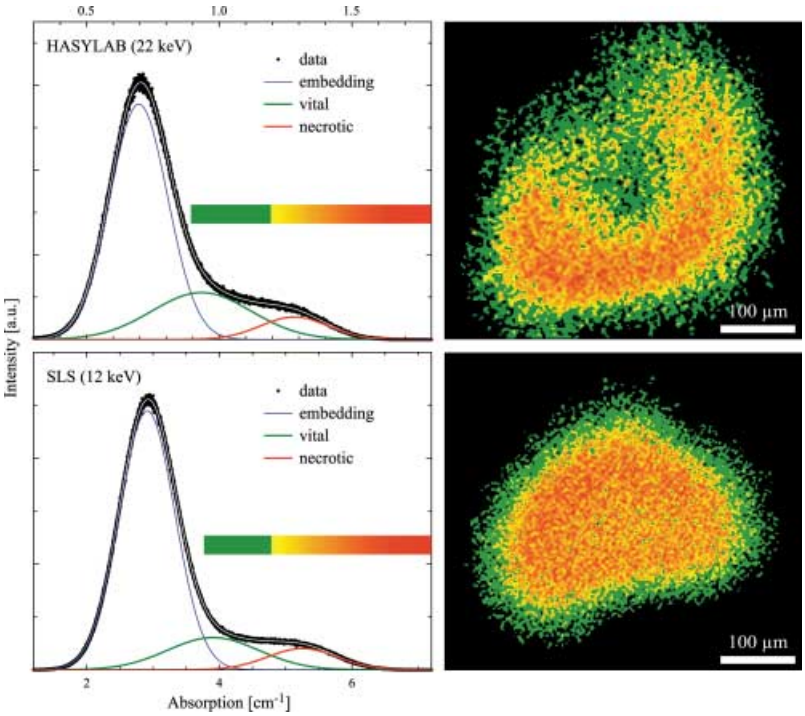

Figure 4. The modification of the staining protocol results in the change of the histograms, but the fit with 3 Gaussians is again perfect. There is, however, a transition range of lower absorption, which changes the cell peak to a shoulder of the peak associated to the embedding material. The transition peak green colored is related to an area at the cluster's periphery about 50 to 100 μm wide.

virtual cuts are not fully identical, but they qualitatively show the higher resolution power of the third generation source. Even the tomogram from this source, however, may only allow segmenting individual cells in the region on the right, where the cell cluster is less dense.

To identify the individual cells, we have applied a different protocol to stain the cells in a more specific way, that is, to stain the DNA and RNA by osmiumammine-B. Figure 4 shows the results for the DNA/RNA-stained cell cluster in a fashion very similar to that in Figure 3 for the conventional membrane staining. The peaks, here, are not as well separated as in Figure 3. The peaks associated with the cells are rather a shoulder, which cannot be described by one Gaussian. The fit using three Gaussians, as was done for the membrane staining, describes very well the histograms for the tomograms obtained at the beamlines W2 (HASYLAB at DESY) and 4S (SLS at PSI). The related slices, represented on the right in Figure 4, show a different behavior with respect to the slices in Figure 3. The region of lower density at the periphery about 50 μm wide surrounds the core of much higher absorption. The transition is rather discontinuous. One might find features of typical cell size, but the reproducible segmentation of cells is difficult or rather impossible.

Such HEK 293 cell clusters were also characterized by 2D images of fluoroscopy and phase-contrast microscopy after histology, as shown in Figure 5. Both images illustrate the behavior that the cell cluster consists of two different parts, the core and the shell. The fluoroscopic image, which shows the cell cluster after 86 days of culturing, proves the viability of the cells at the periphery by the green FDA color originating from the esterase activity. In the center of these relatively large cell clusters, one finds the PI color related to the nonvital cells. The other image below shows the histological slice, where the cells are colored by hematoxylin/eosin. This phase-contrast image, also acquired with a

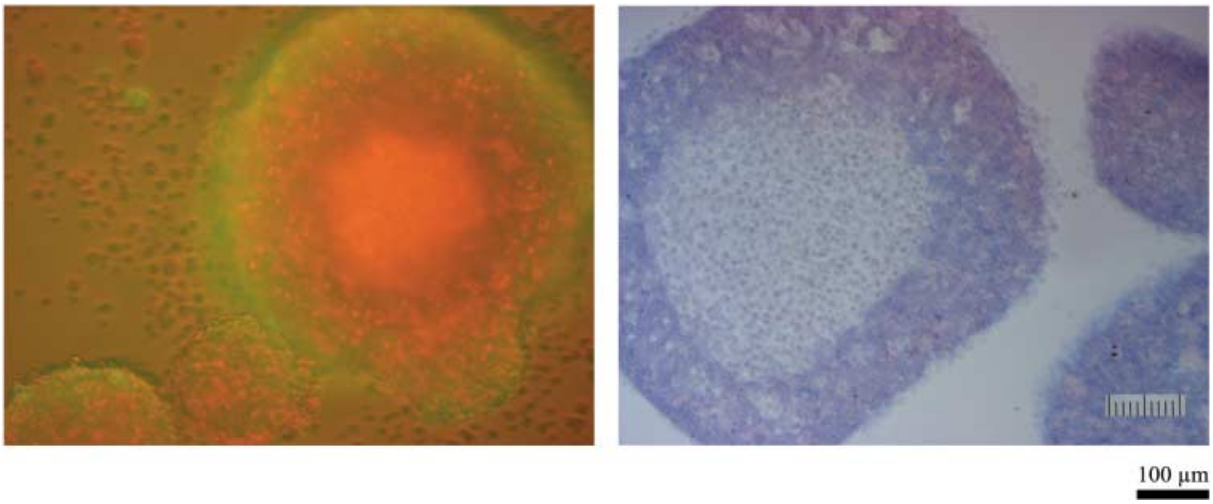

Figure 5. The HEK 293 cell clusters are characterized by 2D images of fluoroscopy and phase-contrast microcopy after histology. Both images illustrate the separation of the cell cluster in core and shell. The fluoroscopic image proves the viability of the cells at the periphery by the green FDA color from the esterase activity. The cores of the relatively large cell clusters exhibit the PI color related to the nonvital cells. The image below is a histological slice colored by hematoxylin/eosin. This phase-contrast image shows small, bright areas in the center and a well-separated darker outer part of the spheroid. Hematoxylin leads to the violet color in RNA-rich areas. Consequently, the core has a lower RNA density with respect to the shell.

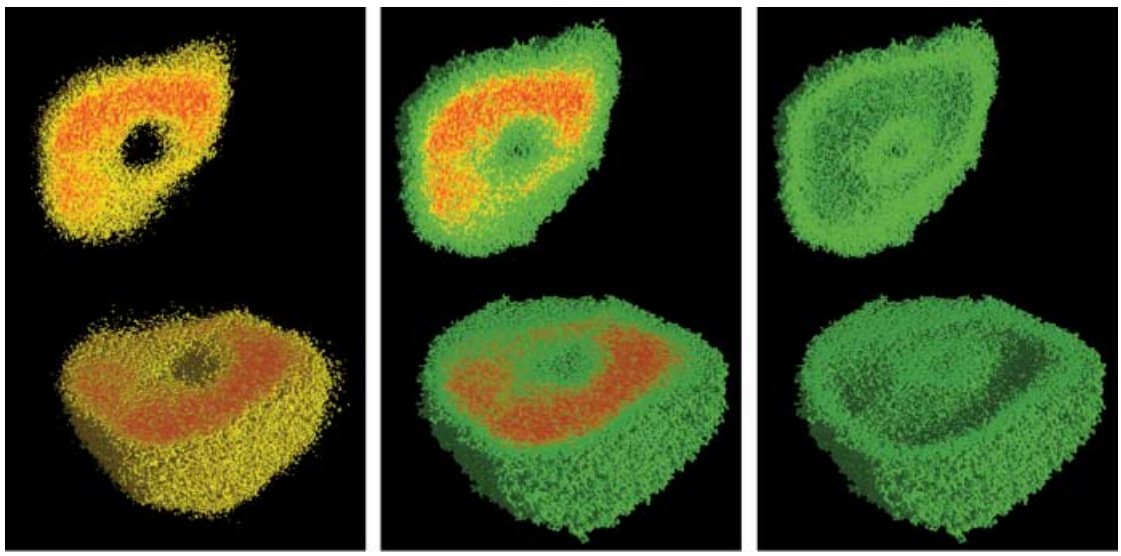

Figure 6. In the center of the figure one segmented cell cluster is represented. The colors correspond to the local absorption values given by the color bar in Figure 4. On the left-hand side the core and on the right-hand side the shell of the cluster have been extracted. The volume of both parts is almost identical.

magnification of 200, exhibits small, bright areas in the center of the cluster and a well-separated darker outer part of the spheroid. Hematoxylin leads to the violet color in RNA-rich areas. Thus the core contains less RNA with respect to the shell.

These results and the ones gained from the tomograms of the DNA/RNA-stained cell cluster (cf. Figs. 4 and 5) reveal that the HEK 293 cell clusters consist of vital cells at the periphery and nonvital cells with high DNA density in the center. To quantify the vital part on the basis of the 3D data sets, we segmented both core and shell to determine their volume, as qualitatively shown by the 3D representations in Figure 6. The values for the tomogram of the beamline 4S (SLS at PSI) are 53% vital cells, whereas the

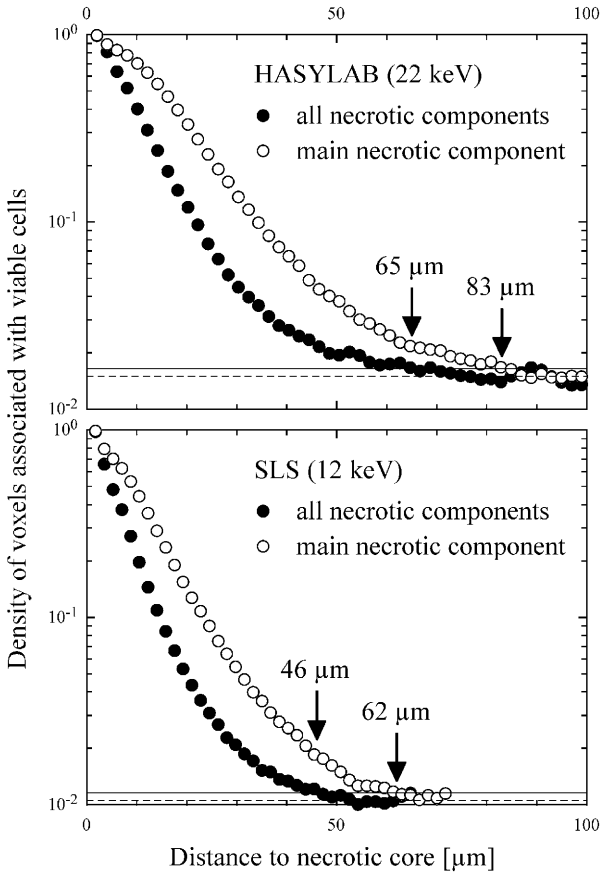

Figure 7. The thickness of the rim of viable cells is resolved by voxel-wise increasing the main necrotic component (open circles) and all necrotic components (filled circles) until a value of 10% (solid line) above the noise level (dashed line) is reached. Therefore, the filled circles represent the lower limit of the shell's thickness, whereas the open circles correspond to the lower limit. Assuming a typical cell size of 10 μm, the shell consists of 6 $\pm$ 1 layers of viable HEK 293 cells.

data from the beamline W2 (HASYLAB at DESY) show 65% vital cells.

To achieve quantitative results for the thickness of the vital shell of the clusters, the necrotic part was virtually increased voxel-wise by dilatation steps until all voxels associated with the rim were incorporated. This was done selecting the largest necrotic component, which can be easily identified and corresponds to 98.7% (SLS tomogram) and 98.2% (HASYLAB tomogram) of the voxels exhibiting the related absorption. Using the data of the SLS, after 35 dilatations—equivalent to 62 μm—a value 10% above the noise level was reached, as shown by the open circles in the lower part of Figure 7. The noise level was detected with high precision (dashed line) by counting voxels, thresholded for vital cells, in a region well apart from any cell cluster. The crossing of the data with the solid line, which is 10% above the noise level, is defined as the shell thickness. The HASYLAB tomogram provides a larger value of 83 μm. The same procedure was carried out considering all components (voxels), which exhibit the absorption of the necrotic part (closed circles). These data yield the lower limit of the shell thickness. They are 16 μm and 18 μm, respectively, lower than the calculation for the main component.

Discussion and Conclusion

SRμCT in the absorption contrast mode provides the 3D mapping of the absorption coefficient. The incorporated higher absorbing agents produce the contrast. Consequently, the binding of the contrast agents to selected cell compartments results in a specific staining. It is still unclear if more sophisticated SRμCT methods, which are based on the phase contrast instead of the absorption, could be helpful. For low-weight elements, of which biological tissues consist, the contrast gain using phase contrast instead of absorption can be larger by two to three orders of magnitude (Bonse & Busch, 1996). In general, the contrast originates from the combination of absorption, scattering, reflection, diffraction, and phase shifts. Primarily, the absorption contrast is used. For low-weight materials and the related rather low photon energies of about 10 keV, this is the photoelectric absorption. Here, the X-ray photon energy is completely transferred to a core electron of the absorbing atom. The secondary processes do not significantly contribute to the detected signal. The absorption exhibits the Z^4 dependence (Z atomic number), whereas the phase shift depends almost linearly on Z. The phase shift reflects mainly the total electron density (Rayleigh scattering), which could be described by the refractive index n, as shown for interferometric measurements already in 1965 (Bonse & Hart, 1965*a*, 1965*b*). The contrast contours as a result of the partial coherent beams, which are visible at the synchrotron radiation sources of the third generation, however, are not only dependent on n but show a strong dependence on the gradient of n. Thus, on the one hand, this method is extremely sensitive to any kind of external and internal interfaces. On the other hand, this results in a much more complex reconstruction and quantitative information is often questionable. The interpretation of the 3D structures obtained is, indeed, difficult and, especially for complex-shaped, composite samples, even impossible. For the 3D cell cultures, which mainly consist of water, the variation in the refractive index and its gradient might be so small that also the related contrast is insufficient for cell segmentation. To our best knowledge, however, the experiment using a kind of phase contrast for the 3D characterization of cells in the hydrated environment has not yet been performed. The reason might be the high experimental effort and the stability requirements for sample positioning during the multiple scans (at different sample detector distances). From this perspective SRμCT in absorption contrast mode is now the method of choice. Especially interesting, however, seems to be the combination of both phase contrast and absorption-contrast modes to ob-

tain a more detailed insight into the internal structure of the cells and thereby into the cell's function.

Applying SRμCT to RNA/DNA-stained cells in clusters of submillimeter size, we demonstrate that the shell of the cell cluster exhibits much lower absorption. This means that the density of the DNA/RNA is significantly lower for the outer than for the inner part. Note that the fluorescence images show a higher amount of RNA in the outer part of the cell clusters, implying a very high DNA density in the center of the cell cluster.

One may assume that the lower RNA/DNA density is the result of the preparation, especially the washing after the staining procedure. Simple estimates of the diffusion coefficients reveal that such an effect can be definitely ruled out.

From these observations we conclude that the HEK 293 cell clusters consist of a shell of vital cells at the periphery and a core of nonvital, necrotic cells with a high DNA density in the center. The amount of vital cells (53% and 65%) determined on the basis of the data from the different beamlines (W2, HASYLAB at DESY and 4S, SLS) at different photon energies and setups is reasonable. The remaining difference is the result of quite some ringlike artifacts encountered in the tomogram retrieved from the beamline W2 (HASYLAB at DESY), which enlarge especially the vital part of the cluster.

The exact determination of the thickness of the vital shell is, however, difficult. It is expected that the shell itself consists of three parts, an inner part of small nonproliferating and loosely packed cells, a transition part of smaller nonproliferating and densely packed cells and large proliferating cells in the outer part (Müller-Klieser, 1987; Casciari et al., 1992). Consequently, the absorption is not constant over the vital shell, but especially low near the surface of the cluster. Because the density resolution is already close to the lower limit, the surface is difficult to extract. The methods available usually rely on relatively smooth surfaces, which can be generated by a sequence of dilatation and erosion steps. Here, one has to prove the volume conservation, which is not given *a priori*. The application of the same number of dilatation and erosion steps to the necrotic and the total cell cluster, respectively, leads to a massive change of the ratio between the necrotic part and the vital shell. This change is attributed to the different density resolution for both parts in relation to the background level.

Besides smoothing, a distance transform is often a prerequisite for the quantitative thickness assessment. The rather open structure close to the cluster's surface makes such an analysis questionable. The thickness of the shell is underestimated. Thus, methods for the extraction of model-independent thickness parameters as proposed by Hildebrand and Rüegsegger (1997) are not applicable here.

Consequently, we used a simpler algorithm for the quantitative analysis of the shell thickness based on the assumption that the shell has a constant thickness perpendicular to the cluster's surface. This implies that the necrotic part is self-similar to the entire cluster. The self-similarity assumption is realistic, because the shell thickness is determined by the diffusion of nutrients and other species (Casciari et al., 1992). As a reasonable approach one can virtually increase the necrotic part voxel-wise by dilatation steps until the rim is fully incorporated. Here, the two extreme estimates, mentioned previously, are taken into account. The dilations of the main necrotic component seems to be more reasonable, because the interface between the vital and the necrotic cells in the tomogram is rough due to a limited signal-to-noise ratio and all kinds of artifacts. This means that the actual shell thickness rather corresponds to the values for the main necrotic component given in Figure 7, that is, 62 μm and 83 μm, respectively. The larger value for the HASYLAB setup is explained by the occurrence of ringlike artifacts resulting from defects in the detecting scintillator. In addition, the portion of the necrotic part is 0.5% smaller for the HASYLAB data than for the SLS data, which indicates a higher interface roughness in the tomogram and shifts the shell thickness to larger values. These reflections, however, do not imply that the HASYLAB data are worse, because the density resolution depends on the photon energy, which is much larger for the HASYLAB setup.

Thus the exact value for the thickness of the vital shell should be close to 60 μm. As the cell diameter is about 10 μm, the shell of the cluster investigated corresponds to 6 ± 1 layers of vital cells. This value differs from the thickness of the shell represented by the histological slice in Figure 4. First of all, it has to be noted that the clusters depicted in Figures 5 and 6 are not comparable on a quantitative basis, as the boundary conditions for the cluster preparation were different. Moreover, the histological slice cannot always be cut perpendicular to the cluster's surface because of the nonspherical morphology. Thus, the 2D techniques including classical histology always give rise to larger values than the 3D approaches. The 2D techniques can only provide the upper limit.

In summary, we conclude that SRμCT can be used to determine the nonvital core of a spheroid or toroid cell cluster. The optimal HEK 293 cell cluster diameter, that is, the maximum cluster size without the formation of a nonvital core, which is insufficiently supplied with oxygen and/or other nutrients, corresponds to a maximal 120 μm for the selected culture conditions. Moreover, SRμCT provides the possibility to correlate cell cluster morphology and cell viability to the preferred culture conditions. With the further development and adaptation of promising stains for functional imaging, using SRμCT other features of interest in biological cells can be detected and visualized in 3D space.

Acknowledgments

The financial support from the Schweizerischer Nationalfonds (2153-057127.99) and from the HASYLAB at DESY

(II-00-041 and I-02-068) and the Swiss Light Source at Paul Scherrer Institute (MS020308_12 and 20030152) is gratefully acknowledged.

References

Abbott, A. & Cyranoski, D. (2003). Biology's new dimension. *Nature* **424**, 870–872.

Beckmann, F. (2001). Microtomography using synchrotron radiation as a user experiment at beamlines BW2 and BW5 of HASYLAB at DESY. In *Developments in X-ray Tomography III*, Bonse, U. (Ed.), pp. 34–41. San Diego: SPIE—The International Society for Optical Engineering.

Bernhardt, R., Scharnweber, D., Müller, B., Thurner, P., Schliephake, H., Wyss, P., Beckmann, F., Goebbels, J. & Worch, H. (2004). Comparison of microfocus- and synchrotron X-ray tomography for the analysis of osteointegration around Ti6Al4V-implants. *Eur Cell Mater* **7**, 42–51.

Bonse, U. & Busch, F. (1996). X-ray computed microtomography (μCT) using synchrotron radiation. *Prog Biophys Mol Biol* **65**, 133–169.

Bonse, U. & Hart, M. (1965*a*). An X-ray interferometer. *Appl Phys Lett* **6**, 155–156.

Bonse, U. & Hart, M. (1965*b*). An X-ray interferometer with long separated interfering beam paths. *Appl Phys Lett* **7**, 99–100.

Casciari, J.J., Sotirchos, S.V. & Sutherland, R.M. (1992). Mathematical modelling of microenvironment and growth in EMT6/Ro multicellular tumour spheroids. *Cell Prolif* **25**, 1–22.

Hildebrand, T. & Rüegsegger, P. (1997). A new method for the model-independent assessment of thickness in three-dimensional images. *J Microsc* **185**, 67–75.

Hoffman, R.M. (1993). To do tissue culture in two or three dimensions? That is the question. *Stem Cells* **11**, 105–111.

Kak, A.C. & Slaney, M. (2001). *Principles of Computerized Tomographic Imaging*. Philadelphia, PA: The Society of Industrial and Applied Mathematics.

König, D., Carvajal-Gonzalez, S., Downs, A.M., Vassy, J. & Rigaut, J.P. (1991). Modelling and analysis of 3-D arrangements of particles by point processes with examples of application to biological data obtained by confocal scanning light microscopy. *J Microsc* **161**, 405–433.

Laurent, M., Johannin, G., Gilbert, N., Lucas, L., Cassio, D., Petit, P.X. & Fleury, A. (1994). Power and limits of laser scanning confocal microscopy. *Biol Cell* **80**, 229–240.

Levin-Zaidman, S., Frenkel-Krispin, D., Shimoni, E., Sabanay, I., Wolf, S.G. & Minsky, A. (2000). Ordered intracellular reca–DNA assemblies: A potential site of in vivo reca-mediated activities. *Proc Natl Acad Sci USA* **97**, 6791–6796.

Liu, M., Xu, J., Souza, P., Tanswell, B., Tanswell, A.K. & Post, M. (1995). The effect of mechanical strain on fetal rat lung cell proliferation: Comparison of two- and three-dimensional culture systems. *In Vitro Cell Dev Biol Anim* **31**, 858–866.

Marquardt, D.W. (1969). An algorithm for least-squares estimation of nonlinear parameters. *J Soc Ind Appl Math* **11**, 431–441.

Müller, B., Beckmann, F., Huser, M., Maspero, F., Szekely, G., Ruffieux, K., Thurner, P. & Wintermantel, E. (2002). Non-destructive three-dimensional evaluation of a polymer sponge by micro-tomography using synchrotron radiation. *Biomol Eng* **19**, 73–78.

Müller, B. & Wintermantel, E. (1999). Ein strukturkompatibler Werkstoff für die Leberzelltransplantation. *Bulletin* **274**, 42–45.

Müller-Klieser, W. (1987). Multicellular spheroids. *J Cancer Res Clin Oncol* **113**, 101–122.

Stampanoni, M., Wyss, P., Abela, R., Borchert, G., Vermeulen, D. & Rüegsegger, P. (2001). X-ray tomographic microscopy at the Swiss light source. In *Developments in X-ray Tomography III*, Bonse, U. (Ed.), pp. 42–53. San Diego: SPIE—The International Society for Optical Engineering.

Suzuki, K., Horiba, I. & Sugie, N. (2003). Linear-time connected-component labeling based on sequential local operations. *Comput Vision Image Understand* **89**, 1–23.

Takezawa, T. (2003). A strategy for the development of tissue engineering scaffolds that regulate cell behavior. *Biomaterials* **24**, 2267–2275.

Thurner, P., Beckmann, F. & Müller, B. (2004). An optimization procedure for spatial and density resolution in hard X-ray micro-computed tomography. *Nucl Instrum Meth Phys Res B* **225**, 599–603.

Thurner, P., Müller, B., Beckmann, F., Weitkamp, T., Rau, C., Müller, R., Hubbell, J.A. & Sennhauser, U. (2003). Tomography study of human foreskin fibroblasts on polymer yarns. *Nucl Instrum Meth Phys Res B* **200**, 397–405.

Weaver, V.M., Petersen, O.W., Wang, F., Larabell, C.A., Briand, P., Damsky, C. & Bissell, M.J. (1997). Reversion of the malignant phenotype of human breast cells in three-dimensional culture and in vivo by integrin blocking antibodies. *J Cell Biol* **137**, 231–245.